Fundamental relations between the symmetry of excitation and the existence of spatiotemporal subharmonic structures in a pattern-forming dynamic system

Ralf Stannarius and Jana Heuer
Institut für Experimentelle Physik, Otto-von-Guericke-Universität Magdeburg, Universitätsplatz 2, D-39106 Magdeburg, Germany

Thomas John
Carl-von-Ossietzky-Universität Oldenburg, Institut für Physik, D-26111 Oldenburg, Germany
(Received 20 July 2005; published 29 December 2005)

In electrohydrodynamic convection of nematics, excitation with sine or square waves of period T leads to convection structures in which the charge density, director, and velocity fields perform T-periodic oscillations. Nonconventional waveforms such as sawtooth excitation can lead to patterns with T-periodic as well as T-antiperiodic (subharmonic) dynamics. We consider different classes of excitation fields $E(t)$: such with antisymmetry in the two half periods $E(t)=-E(t+T/2)$, such with time inversion symmetry $E(t)=E(-t)$, and dichotomous waveforms (two alternating values E_1,E_2) and discuss their influence on the pattern dynamics. From the analysis of linear differential equations that describe the system near threshold, we show analytically that each of these conditions inhibits subharmonic dynamics at onset. Numerical and experimental support of these predictions is provided.

DOI: 10.1103/PhysRevE.72.066218 PACS number(s): 05.45.−a, 47.20.−k, 61.30.−v

I. INTRODUCTION

In the field of dissipative pattern formation, nematic electroconvection is among the most comprehensively investigated and thoroughly understood systems. It was discovered about four decades ago independently by Williams and Kapustin [1], and the convection mechanism was later theoretically described by Carr [2] and Helfrich [3]. The classical experiment uses sine or square wave electric excitation fields, where two fundamental dynamic regimes have been early identified, the conduction regime at low-frequency excitation and the dielectric regime at high-excitation frequencies (separated by some cutoff frequency). They are distinguished by the time symmetries of the system variables.

Interestingly, the system of EHC has long been thought to produce only patterns that have the same temporal periodicity as the electric excitation field, unlike many other dynamic systems such as the parametrically excited pendulum [4] or Faraday waves [5–10] that can produce T-periodic as well as T-antiperiodic dynamics. Only recently, it has been shown that a subharmonic EHC regime exists [11,12], e.g., under excitation with certain triangular waveforms. In this regime, the director, charge and velocity fields perform oscillations that are periodic with $2T$ when the excitation has the period T. Patterns in this regime differ from the two classical convection structures not only by their temporal characteristics, but also by the wave length selection mechanism. Since subharmonic EHC structures remained undiscovered for a very long time, it is natural to assume that they are principally excluded for a large class of excitation waveforms because of the particular symmetries of the dynamic equations for the Carr-Helfrich effect.

In this paper, we study some general relations between symmetries of the excitation waveform and the fundamental time response of the system. We consider time-periodic electric driving fields and prove that certain symmetry properties of the excitation field are essential for the formation or inhibition of subharmonic patterns. If the excitation matches at least one of three conditions detailed below, subharmonic patterns are generally inhibited. In the classical experiments with sine or square wave excitation, at least two of these inhibiting conditions are always fulfilled. This is the reason that subharmonic EHC patterns have long remained undetected in the past. A mismatch of all three conditions does not necessarily lead to subharmonic patterns, and we do not exclude that additional inhibiting conditions may exist. However, it is shown in experiments and in numerical calculations that some other symmetry properties of the excitation, for example $E(t)=-E(-t)$, are compatible with the existence of subharmonic patterns.

Apart from the aspect of the completely different pattern dynamics in the subharmonic structures, additional scientific interest lies in the new accessible range of pattern wavelengths, between the large-scale conduction rolls (wave number essentially determined by the container dimensions) and short-scale dielectric rolls (wave number related to material properties), as well as in the investigation of the wavelength selection mechanism. Furthermore, higher instabilities (subharmonic chevrons) and nonlinear interactions between patterns belonging to different regimes in certain coexistence ranges have remained uninvestigated so far.

The paper is structured as follows. In the theoretical part, we provide arguments for description of the EHC dynamics with the particular model, which leads to a linearized differential equation system, and we discuss limitations of the model. Then, we analyze excitation waveforms with certain time symmetries within this model. Similar concepts have been applied in the analysis of solutions of differential equation systems, e.g., by Schulze [13]. Using different mathematical approaches, we derive three driving conditions for inhibition of subharmonic patterns, and an additional condition on material parameters (dielectric anisotropy). Finally,

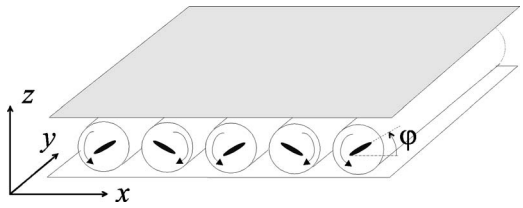

FIG. 1. Sketch of the cell geometry with convection rolls (normal rolls), velocity and director fields, and the definition of the coordinate system.

we discuss the structure of stability diagrams on the basis of numerical calculations and present experimental data that support the theoretical predictions.

II. THEORETICAL MODEL

For the description of the fundamental electroconvection dynamics, we use a simple differential equation system for the two coupled system variables, the space charge density $\tilde{q}$ and the director deflection $\tilde{\varphi}$ in the liquid crystal cell. Other dynamic variables, including the convective flow field, are linearly coupled in their temporal behaviour to one of these two system variables. The flow field amplitude is proportional to the director deflection amplitude, since inertial effects can usually be neglected in the thin cells.

The differential equations used here have been derived from the Maxwell and Navier-Stokes equations, and the balance of torques on the nematic director [14–19]. We apply here the simplified two-dimensional description, i.e., director, flow, and charge fields are assumed to be uniform in the direction y normal to the ground-state director orientation in the cell plane (normal rolls). The director field is assumed to deflect only in the plane formed by the preferential director alignment axis x and the cell normal z (Fig. 1). This is the common situation mostly encountered in our experiments near the convection threshold. Only at very low frequencies can the first instability in the experiment be oblique rolls with a component of the wave vector along y.

It has to be mentioned here that much more elaborated theoretical models are available today, which describe the complexity of EHC patterns in much greater detail (see progress in the theoretical analysis, e.g., in Refs. [20–31]). For special excitation waveforms such as sine waves, analytical expressions for the neutral curves have been derived. Further progress has been the discussion of different test functions for the dynamic variables, and inclusion of flexoelectric terms [22,24]. These theoretical improvements are able to describe oblique and abnormal rolls (wave vector or director components in the third dimension) by a complete three-dimensional ansatz of the spatial structure of the dynamic variables [23–25]. The origin of traveling rolls at onset has been described by a weak-electrolyte model where the ionic mobilities are taken into account [26,27]. Pretilted director anchoring can be considered [28]. Ginzburg-Landau amplitude equations for a weakly nonlinear description have been worked out [22,24,31]. Higher instabilities have been treated theoretically, e.g., Refs. [30,32]. Reviews of these theoretical achievements can be found, for example, in Refs. [20,21,29].

In view of the availability of these improved models, it seems appropriate to discuss the relevance of the simple model considered in this work, and to evaluate its merits and shortcomings, before the equations are further analyzed. The main advantage and attractiveness of the model used here is its evident simplicity as well as its appropriateness to describe all basic dynamic features, pattern stability diagrams, threshold fields and wave numbers with sufficient accuracy. Several details are not included, for example, possible flexoelectric terms. Further, we do not consider the three dimensionality of the patterns. This is appropriate as long as the experiments confirm the formation of normal rolls at the pattern onset, i.e., the wave vector of the rolls has only components in the plane formed by cell normal and the director surface alignment axis. Since we perform a linear analysis, we detect only the thresholds for the driving parameters and cannot make statements about higher instabilities. Strictly, the dynamic description is only correct at the threshold. The most serious problem is the choice of test functions, which yield unrealistic boundary conditions for the flow field. The harmonic ansatz which considers only the ground mode normal to the cell plane satisfies free boundary conditions for the velocity component parallel to the electrodes. Other test functions can in principle be used, as has been demonstrated in Refs. [22,24]. The choice of the spatial test functions will, however, not influence the qualitative dynamic behavior of the system. Quantitatively, it may lead to slight systematic mismatches of calculated and experimental threshold voltages and wave numbers. As earlier experiments have shown that our model reproduces the experimental measurements consistently and with satisfactory accuracy, we sacrifice the complications related to more complex description in favor of a most achieveable simplicity of the model. An incorporation of other, more realistic test functions will certainly be possible and will lead to the same structure of the differential equation system with slight quantitative differences in the parameters. The symmetries in the dynamic equations that are exploited in the analysis are not influenced by the choice of better test functions. In particular, an extension to oblique rolls would not affect the symmetry properties under consideration. They will be modified when flexoelectric terms enter the equations, but such terms will also affect the symmetries of conduction and dielectric regimes [28]. In most experiments, such terms are commonly neglected. For the purpose of this paper, the model serves well to give insight into the basic mechanisms leading to structures with different time symmetries of the dynamic variables for the standard experiment with planar parallel anchoring at both cell plates.

III. MODEL EQUATIONS

We use a test mode ansatz that splits the two dynamic variables, the charge density $\tilde{q}(\vec{r},t)$ and the director deflection respective to the x axis $\tilde{\varphi}(\vec{r},t)$ into a spatially modulated part and a time-dependent amplitude

$$\tilde{q}(x,z,t) = q(t)\sin(k_x x)\cos(k_z z),$$

$$\tilde{\varphi}(x,z,t) = \varphi(t)\cos(k_x x)\cos(k_z z), \quad (1)$$

where d is the cell thickness and $k_z = \pi/d$. The further analysis deals with the time evolution of the amplitudes $\varphi(t)$ and $q(t)$. It is described by two coupled ordinary differential equations (ODE's) of the form

$$\frac{d}{dt}\vec{Z}(t) = \mathbf{A}(t)\vec{Z}(t), \quad (2)$$

with

$$\vec{Z}(t) = \begin{pmatrix} q(t) \\ \varphi(t) \end{pmatrix}, \quad \mathbf{A}(t) = \begin{pmatrix} A_1 & A_2 E(t) \\ A_3 E(t) & A_4 + A_5 E^2(t) \end{pmatrix}. \quad (3)$$

Both equations are linear in φ and q. The coefficients A_i contain liquid crystal material parameters, wave numbers of the test mode and cell parameters (see the Appendix). The electric field is time periodic with period T, $E(t)=E(t+T)$, and consequently $\mathbf{A}(t)=\mathbf{A}(t+T)$. We may write the matrix $\mathbf{A}(t)$ in a general form

$$\mathbf{A}(t) = \begin{pmatrix} a_{11}(t) & a_{12}(t) \\ a_{21}(t) & a_{22}(t) \end{pmatrix}.$$

This ODE system has a fundamental solution of the form

$$\vec{Z}(t) = \mathbf{P}(t)\vec{Z}(0), \quad (4)$$

with the 2×2 matrix $\mathbf{P}(t)$ that fulfills the matrix equation $\dot{\mathbf{P}}(t)=\mathbf{A}(t)\mathbf{P}(t)$, and $\mathbf{P}(0)=\mathbf{E}$ is the unit matrix. In the case when $\mathbf{A}$ is time independent, the ODE system (2) reduces to a system with constant coefficients with the solution $\mathbf{P}(t)=\exp(\mathbf{A}t)$. This can be exploited to compose analytical solutions for piecewise constant excitation waveforms, such as square or superimposed square waves [11].

For a time-periodic matrix $\mathbf{A}(t+T)=\mathbf{A}(t)$, the Floquet theorem yields the particular form $\mathbf{P}(t)=\mathbf{R}(t)\exp(\mathbf{B}t)$, with $\mathbf{R}(t)=\mathbf{R}(t+T)$ and $\mathbf{B}=$const. The regular transfer matrix $\mathbf{M}=\exp(\mathbf{B}T)$ determines the evolution during one excitation field period $\mathbf{P}(t+T)=\mathbf{P}(t)\mathbf{M}$. The eigenvalues of $\mathbf{M}$, the characteristic multipliers μ_i, are related to the trace $\mathrm{Tr}(\mathbf{M})$ and the determinant $\det(\mathbf{M})$ of the transfer matrix by

$$\mu_{1,2} = \frac{1}{2}[\mathrm{Tr}(\mathbf{M}) \pm \sqrt{[\mathrm{Tr}(\mathbf{M})]^2 - 4\det(\mathbf{M})}]. \quad (5)$$

A necessary and sufficient condition for asymptotic stablility is that both $|\mu_i|<1$. In the following, we sort the characteristic multipliers so that $|\mu_1|\geq|\mu_2|$.

When the elements of $\mathbf{A}$ are not constant, the determination of the matrix $\mathbf{M}$ is not straightforward, and there is no simple relation between the elements of $\mathbf{A}(t)$ and the multipliers μ_i [33]. However, it is well known for homogeneous ODE systems such as Eq. (2), that [34]

$$\det(\mathbf{M}) = \mu_1\mu_2 = \exp\left(\int_0^T \mathrm{Tr}\mathbf{A}(t)dt\right). \quad (6)$$

In the standard EHC model, the matrix $\mathbf{A}(t)$ has only real coefficients, thus $\det(\mathbf{M})$ is positive according to Eq. (6). As a consequence, both eigenvalues are either real or complex conjugated, their real parts have the same sign. Since the elements of $\mathbf{A}$ depend upon several experimental and material parameters, in particular on the wave number k_x of the test mode and the electric field $E(t)$, the characteristic multipliers that determine the type of solutions may depend upon these parameters in a complex way. Even though the ODE system in Eq. (2) may have some superficial similarity with the parametrically driven pendulum equations, it is evident that it is far more complex because a stability analysis for certain excitation parameters involves the consideration of the full wave number spectrum in k_x (or even in the two wave numbers k_x and k_y if the equations are generalized to oblique roll patterns). Moreover, all four matrix elements are, in general, nonzero in the EHC system, and the two nondiagonal elements as well as one of the diagonal elements depend upon the excitation parameter.

In order to determine the stability of the ground state at a given "simple" excitation waveform (e.g., sine, triangular, or square waves of fixed frequency) numerically, one can characterize the excitation by the electric field amplitude E_0 and calculate the characteristic multipliers in the two-parameter diagram of E_0 and wave number k_x. For more complex excitation schemes, such as those considered in the following, it is useful to fix all parameters of the driving field except one and to calculate the stability in a two-parameter diagram of one electric field parameter and the wave number k_x. For example, at superposition of two square waves one amplitude, the two frequencies and the mutual phase shift are fixed and the second amplitude is used as the parameter. From a set of stability diagrams, two- or more-dimensional pattern state diagrams can be constructed (see below, Sec. VIII). With respect to the recognition of subharmonic patterns, this has been demonstrated in earlier work [11,12].

In parameter ranges where both μ_i are real and positive, the differential equation system has T-periodic solutions. When the two eigenvalues are real and negative, the system has T-antiperiodic solutions. In both cases, the envelopes of these solutions grow ($|\mu_1|>1$) or decay ($|\mu_1|<1$) exponentially. In case of complex multipliers, the system exhibits solutions with periods that are in general incommensurate with the excitation frequency. In our particular system ($\varepsilon_a=\varepsilon_\parallel-\varepsilon_\perp<0$, see the Appendix), the trace of $\mathbf{A}$ is negative for all E and all k_x. It follows from Eq. (6) that the product $\mu_1\mu_2$ is smaller than 1. When the two eigenvalues are complex conjugated, their absolute values are equal, thus both are smaller than 1. This ensures that the ground state is stable in the parameter range where the μ_i are complex, and we do not need to consider this narrow transition region (around the separatrix $\mathcal{S}$ in the diagrams shown below) in the stability analysis.

The neutral curve $\mathcal{N}$ is given by $\mu_1=\pm 1$. When $|\mu_1|<1$ for all k_x at a given excitation parameter, the ground state is

stable. Otherwise the threshold field and critical wavelength are given by the global minimum E_0 of the neutral curve in the (E_0, k_x) plane. When this minimum is located in a section of $\mathcal{N}$ with $\mu_1=-1$, subharmonic patterns appear at onset, otherwise the classical dielectric or conduction patterns form the first instability. For some combinations of waveform, material and cell parameters, there are regions with growing or decaying subharmonic solutions in the (E_0, k_x) plane, but the global minimum of the neutral curve remains in the region of $\mu_1=+1$. Then, subharmonic patterns are not observed in the experiment but one cannot exclude in general that for other cell or material parameters, subharmonic patterns may be found. On the other hand, there are excitation waveforms, for which subharmonic solutions do not exist at all, because of certain symmetry properties of the excitation. Such conditions will be tested in the following. It turns out that essentially the special structure of the nondiagonal elements of the matrix $\mathbf{A}(t)$, $a_{12}=A_2E(t)$ and $a_{21}=A_3E(t)$ are of importance for the following calculations. Three different conditions for the excitation waveform will be considered separately. Since we do not make other assumptions about the properties of $\mathbf{A}$ other than the symmetry conditions specified, the calculations may be easily adopted to any other pattern forming dynamic system with similar symmetries of the dynamic equations.

IV. ANTISYMMETRY IN THE TWO HALF PERIODS OF THE EXCITATION

First, we test the properties of the fundamental solution of Eq. (2) for an excitation field with $E(t)=-E(t+T/2)$. Such an excitation field symmetry leads to

$$\mathbf{A}(t+T/2)=\begin{pmatrix} a_{11}(t) & -a_{12}(t) \\ -a_{21}(t) & a_{22}(t) \end{pmatrix}.$$

For the elements of $\mathbf{P}$ in Eq. (4) after one half period $t=T/2$, we use the notation

$$\mathbf{P}(T/2)=\begin{pmatrix} p_{11} & p_{12} \\ p_{21} & p_{22} \end{pmatrix}.$$

Since all elements a_{ij} are real, the elements p_{ij} are real as well. The fundamental matrix solution in the second half period of the excitation differs from $\mathbf{P}(T/2)$ only by the sign of the off-diagonal elements p_{12} and p_{21}. We substitute

$$\mathbf{A}(t+T/2)=\mathbf{D}^{-1}\mathbf{A}(t)\mathbf{D}, \quad \mathbf{D}=\mathbf{D}^{-1}=\begin{pmatrix} 1 & 0 \\ 0 & -1 \end{pmatrix}$$

and introduce $\vec{\zeta}(t)=\mathbf{D}\vec{Z}(t+T/2)$. Then, the equations $\dot{\vec{Z}}(t+T/2)=\mathbf{A}(t+T/2)\vec{Z}(t+T/2)$ transforms to the ODE's $\dot{\vec{\zeta}}(t)=\mathbf{D}\cdot\mathbf{A}(t+T/2)\mathbf{D}^{-1}\vec{\zeta}(t)=\mathbf{A}(t)\vec{\zeta}(t)$. These equations have the same coefficients as those for $\vec{Z}(t)$, and therefore lead to the same fundamental matrix solution $\vec{\zeta}(T/2)=\mathbf{P}(T/2)\vec{\zeta}(0)$. After the reverse transformation $\vec{Z}(T)=\mathbf{D}^{-1}\zeta(T/2)$ one obtains

$$\vec{Z}(T)=\mathbf{D}^{-1}\cdot\mathbf{P}\left(\frac{T}{2}\right)\mathbf{D}\vec{Z}\left(\frac{T}{2}\right)=\mathbf{Q}\left(\frac{T}{2}\right)\vec{Z}\left(\frac{T}{2}\right)$$

with

$$\mathbf{Q}\left(\frac{T}{2}\right)=\begin{pmatrix} p_{11} & -p_{12} \\ -p_{21} & p_{22} \end{pmatrix}.$$

This result is trivial. If one changes the sign of one of the dynamic variables, leaving the other variable unchanged, the signs of the coupling coefficients in the matrices are inverted. This reproduces but the standard result in EHC, either charge density or director deflection are antiperiodic in $T/2$, while the respective other quantity is periodic in the half cycles. After a full cycle T of the excitation $\vec{Z}(T)=\mathbf{M}\vec{Z}(0)$, where $\mathbf{M}=\mathbf{Q}(T/2)\mathbf{P}(T/2)$ has the form

$$\mathbf{M}=\begin{pmatrix} p_{11}^2-p_{12}p_{21} & p_{12}(p_{11}-p_{22}) \\ p_{21}(p_{22}-p_{11}) & p_{22}^2-p_{12}p_{21} \end{pmatrix}. \tag{7}$$

Without explicitely calculating these terms, one recognizes the type of solutions immediately. The sum of both characteristic multipliers [cf. Eq. (5)]

$$\mu_1+\mu_2=\mathrm{Tr}(\mathbf{M})=(p_{11}-p_{22})^2+2\,\det[\mathbf{P}(T/2)] \tag{8}$$

is always positive because

$$\det[\mathbf{P}(T/2)]=\exp\left(\int_0^{T/2}\mathrm{Tr}[\mathbf{A}(\tau)]d\tau\right)>0.$$

Since it has been derived already from Eqs. (5) and (6) that the signs of the real parts of both multipliers are equal, none of them can have a negative real part, and consequently subharmonic solutions are excluded.

In conclusion, if the two off-diagonal elements of the matrix $\mathbf{A}$ have the time symmetry $a_{ij}(t)=-a_{ij}(t+T/2)$, i.e., under the condition $E(t)=-E(t+T/2)$, the EHC system cannot have subharmonic solutions. All solutions can be classified as the standard conduction or dielectric patterns, with $q(t)=-q(t+T/2)$, $\varphi(t)=\varphi(t+T/2)$ or vice versa [36]. This excludes, among other waveforms, subharmonic patterns at dc free sine or square wave excitation, excitation with antisymmetric triangular waves, and all superpositions of sine or square waves with odd integer frequency ratios.

V. TIME REVERSAL SYMMETRY

We consider now excitation fields that have time reversal symmetry, i.e., waveforms where one can define a time t_0 such that $E(t)=E(t+T)=E(t_0-t)$. In order to show that such waveforms also inhibit subharmonic patterns, we focus on another property of the off-diagonal elements of $\mathbf{A}$. The time dependence of the electric field is contained in these elements in a peculiar way. Both a_{12} and a_{21} are linearly proportional to $E(t)$, thus they have the same time dependence, they differ only by a constant factor. We can consequently symmetrize $\mathbf{A}$ by rescaling the variable $q(t)$ to the dimensionless quantity $\hat{q}(t)=\sqrt{a_{21}/a_{12}}q(t)=\sqrt{A_3/A_2}q(t)$, and set $a=\sqrt{a_{21}a_{12}}\cdot\mathrm{sgn}(E)=\sqrt{A_2A_3}E$:

$$\mathbf{A}(t) = \begin{pmatrix} a_{11}(t) & a(t) \\ a(t) & a_{22}(t) \end{pmatrix},$$

and we choose the time axis such that $t_0=0$. If we split one excitation period into infinitesimally small time intervals in which $\mathbf{A}$ can be treated as constant, then one can integrate the ODE system with constant coefficients in each of these intervals

$$\vec{Z}(t_{i+1}) = \exp(\mathbf{A}_i \delta t_i)\vec{Z}(t_i),$$

with

$$\delta t_i = t_{i+1} - t_i, \quad \mathbf{A}_i = \begin{pmatrix} a_{11}(t_i) & a(t_i) \\ a(t_i) & a_{22}(t_i) \end{pmatrix}.$$

We now set $\mathbf{P}_i=\exp(\mathbf{A}_i\delta t_i)$. As a consequence of the symmetry of the $\mathbf{A}_i$, the matrices $\mathbf{P}_i$ are also symmetrical. The fundamental solution for the half-period $(0,T/2)$, $\vec{Z}(T/2)=\mathbf{P}(T/2)\vec{Z}(0)$, is given by the product of the $\mathbf{P}_i$ of all infinitesimal intervals:

$$\mathbf{P}(T/2) = \lim_{N\to\infty} \mathbf{P}_N \cdot \mathbf{P}_{N-1} \cdot \cdots \cdot \mathbf{P}_2 \cdot \mathbf{P}_1,$$

with $\delta t_i \to 0$ and $\Sigma_i \delta t_i = T/2$.

Now, we calculate $\vec{Z}(0)$ from $\vec{Z}(-T/2)$. Because of the assumed symmetry $\mathbf{A}(t_i)=\mathbf{A}(-t_i)$ and $\mathbf{P}(t_i)=\mathbf{P}(-t_i)$, the matrices $\mathbf{P}_i$ have to be multiplied in exactly reversed order to yield the solution $\vec{Z}(0)=\mathbf{Q}\vec{Z}(-T/2)$,

$$\mathbf{Q}(T/2) = \lim_{N\to\infty} \mathbf{P}_1 \cdot \mathbf{P}_2 \cdot \cdots \cdot \mathbf{P}_{N-1} \cdot \mathbf{P}_N.$$

A product of N matrices has the property $\{\mathbf{P}_1\cdot\mathbf{P}_2\cdot\cdots\cdot\mathbf{P}_N\}^T = \mathbf{P}_N^T\cdot\cdots\cdot\mathbf{P}_2^T\cdot\mathbf{P}_1^T$ and the product of symmetric matrices $\mathbf{P}_i = \mathbf{P}_i^T$, in particular, gives $\{\mathbf{P}_1\cdot\mathbf{P}_2\cdot\cdots\cdot\mathbf{P}_N\}^T = \mathbf{P}_N\cdot\cdots\cdot\mathbf{P}_2\cdot\mathbf{P}_1$. Thus, $\mathbf{Q}(T/2)=\mathbf{P}^T(T/2)$, i.e., the fundamental matrices in the two half periods represent transposed matrices of each other. We combine $\vec{Z}(T/2)=\mathbf{P}(T/2)\vec{Z}(0)$ and $\vec{Z}(0)=\mathbf{P}^T(T/2)\vec{Z}(-T/2)$ to

$$\vec{Z}(T/2) = \mathbf{P}(T/2)\mathbf{P}^T(T/2)\vec{Z}(-T/2)$$

and

$$\mathbf{M} = \mathbf{P}\cdot\mathbf{P}^T = \begin{pmatrix} p_{11}^2 + p_{12}^2 & p_{11}p_{21} + p_{12}p_{22} \\ p_{11}p_{21} + p_{12}p_{22} & p_{22}^2 + p_{21}^2 \end{pmatrix}.$$

The trace of the matrix $\mathbf{M}$ as the sum of the two characteristic multipliers, is

$$p_{11}^2 + p_{12}^2 + p_{21}^2 + p_{22}^2 > 0.$$

As in the previous section, $\mathbf{M}=\mathbf{P}(T/2)\mathbf{P}^T(T/2)$ has either two positive real eigenvalues or two complex conjugated eigenvalues with positive real parts. Subharmonic solutions are excluded for this type of excitation, too. There are only T-periodic solutions if the eigenvalues are real, or oscillating solutions otherwise. Since the expansion of the excitation waveform is done into infinitesimally small intervals, the result holds for arbitrary waveforms that match the time inversion symmetry condition.

Summarizing, if the two off-diagonal elements of $\mathbf{A}(t)$ have the symmetry $a_{ij}(t)=a_{ij}(t_0-t)$ for a certain t_0, i.e., the excitation field symmetry is $E(t)=E(t_0-t)$ in the EHC system, subharmonic solutions cannot exist as a consequence of the structure of $\mathbf{A}(t)$ given in Eq. (3). Such symmetry of $E(t)$ is found at sine or square wave excitation with and without dc offset, at superposition of two square waves with odd integer frequency ratio and zero phase shift (positive slope of the slow frequency coincides with a positive slope of the high frequency) and superposition of two square waves with even frequency ratio but 90° phase shift between both components, also for all types of periodic rectangular pulses (constant E_1 in an interval $0<t<t_1$ and E_2 in the interval $t_1<t<T$), with and without dc offset.

VI. DICHOTOMOUS WAVEFORMS

Finally, we consider the case of dichotomous waveforms, i.e., waveforms that consist of arbitrary periodic sequences of intervals with constant E with only two possible values E_1 and E_2. The waveforms may have dc offset or not. The discussion is based on the observation that both dynamic variables have to change their signs in the subharmonic regime after one period T of the excitation. It will be shown that this is impossible when the waveform is dichotomous.

The symmetrisized equation system is rewritten in polar coordinates by a transformation from $\hat{q}$, φ to r, ϕ:

$$r = \sqrt{\hat{q}^2 + \varphi^2} = \sqrt{\frac{A_3}{A_2}q^2 + \varphi^2}, \quad \tan\phi = \frac{\varphi}{\hat{q}}.$$

The two resulting nonautonomous equations are [19]

$$\dot{r} = g[E(t),\phi]r = \left(\frac{a_{11}+a_{22}}{2} + \frac{a_{11}-a_{22}}{2}\cos 2\phi + a\sin 2\phi\right)r, \tag{9}$$

$$\dot{\phi} = h[E(t),\phi] = a\cos 2\phi + \frac{(a_{22}-a_{11})}{2}\sin 2\phi. \tag{10}$$

Both functions g and h are independent of r, and since Eq. (9) is linear in r, it can be integrated immediately,

$$r(t) = r(0)\exp\left\{\int_0^t g[E(\tau),\phi]d\tau\right\}. \tag{11}$$

We concentrate on the differential equation for ϕ, which describes the relation between charge field and director field, and we look for the phase flow, the fixpoints and their stability. It is useful to introduce for convenience the quantities Ω and ϕ_S with

$$\Omega = \sqrt{(a_{11}-a_{22})^2 + 4a^2}, \quad \tan 2\phi_S = \frac{2a}{a_{11}-a_{22}}, \tag{12}$$

such that Eq. (10) adopts the form

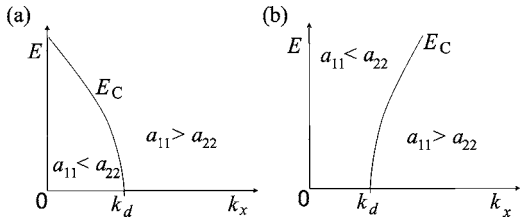

FIG. 2. The line sketches qualitatively the field strength $E_C(k_x)$ where the denominator in Eq. (12) changes its sign, k_d is the wave number at which $A_1=A_4$. The two graphs represent the cases of (a) negative dielectric anisotropy ($\varepsilon_a<0$, $A_5<0$), the standard situation and (b) positive dielectric anisotropy ($\varepsilon_a>0$, $A_5>0$).

$$\dot{\phi} = \frac{\Omega}{2} \sin 2(\phi - \phi_S). \tag{13}$$

Both Ω and ϕ_S are functions of the momentary electric field. In the periods where the electric field is constant, there is an analytical solution

$$\tan(\phi - \phi_S) = \tan[\phi(t_0) - \phi_S] e^{\Omega(t-t_0)}. \tag{14}$$

Fixed points are $\phi=\phi_S+n\pi/2$, $(n=0,1,2,\ldots)$. The coefficient a has the same sign as the electric field E, and depending upon the sign of $a_{22}-a_{11}$ (see Fig. 2), the angles $2\phi_S$ will be found in different quadrants. It will become evident later that for square waves composed of electric fields E_0 and $-E_0$, the region to the left of the curve $E_C(k_x)$ in Fig. 2 corresponds to solutions where the electric charges alternate with the field (conduction patterns), the region to the right corresponds to dielectric solutions (alternating director deflection φ). In terms of the coefficients A_i introduced in Eq. (3) and specified in the appendix, the $E_C(k_x)$ curve is defined by $E_C=\sqrt{(A_1-A_4)/A_5}$ for all k_x, where $(A_1-A_4)/A_5>0$.

Figure 3 sketches the location of the fixed points and their stability and the phase flow field in the interval $-\pi/2 \leqslant \phi \leqslant \pi/2$ in dependence upon the electric field strength E_0. The stable fixed points pass $-\pi/4$ or $\pi/4$, respectively, at E_C. In the following, we will only discuss the standard case $\varepsilon_a<0$, the case $\varepsilon_a>0$ can be treated analogously [37].

From the flow diagrams of Fig. 3, one can construct the qualitative phase flow for special waveforms: Figure 4 shows two possible scenarios when the excitation field is composed of only two values, E_1 and E_2. In the first case (a) the absolute values of both fields are found to the left of the $E_C(k_x)$ curve in Fig. 2 and $|\phi_S(E_1)-\phi_S(E_2)|>\pi/2$, in the second case (b) they are to the right of that curve, $|\phi_S(E_1)-\phi_S(E_2)|<\pi/2$. All other cases with $|E_1|>E_C>|E_2|$ are qualitatively similar to one of the two scenarios presented in Fig. 4, depending upon the value of $|\phi_S(E_1)-\phi_S(E_2)|$.

The figure demonstrates that for any excitation waveform composed of two constant electric fields E_1 and E_2, independent of the sequence and duration of the periods, there are ranges of ϕ where the flow is unidirectional at all times (thick arrows at the right border of the images). In regions with only inward flow at the boundaries (hatched in Fig. 4), trajectories of $\phi(t)$ are "trapped" (see Ref. [19]). The width

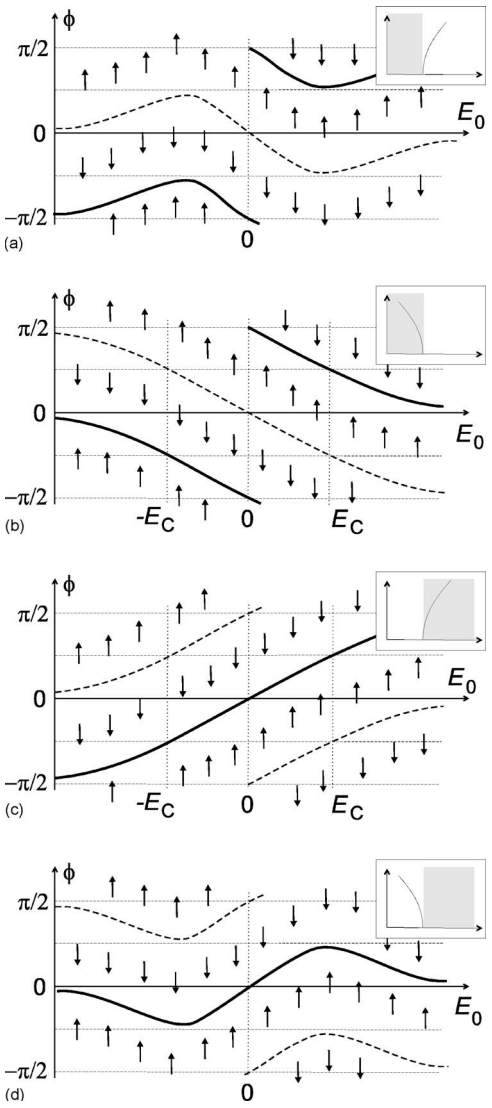

FIG. 3. The figure sketches qualitatively the phase flow in dependence upon the electric field strength E_0 and the positions of the fixed points $\phi_S+n\pi/2$. The insets indicate which part of the (E_0,k_x) plane the diagrams belong to (cf. Fig. 2), test mode wave lengths are $k_x<k_d$ in (a) and (b), $k_x>k_d$ in (c) and (d). Stable fixed points are indicated by solid lines, unstable fixed points by dashed lines. (b) and (d) describe the standard situation $\varepsilon_a<0$, (a) and (c) belong to the case $\varepsilon_a>0$.

of the traps is always narrower than $\pi/2$, consequently the solutions $\phi(t)$ are confined to one or two quadrants and (at least) one of the system variables keeps its sign. In Fig. 4, the grey areas mark regions with unidirectional flow, and the hatched areas mark regions with inflow only, these areas trap the trajectories $\phi(t)$. In Fig. 4(a), $|E_1|$, $|E_2|<E_C$, the $\phi(t)$ curve oscillates around $(n+1/2)\pi$, where $\cos\phi$ changes its sign and consequently, the charge amplitude $q(t)\propto\cos\phi(t)$ alternates with the electric field (conduction regime). In the situation shown in image Fig. 4(b), $|E_1|$, $|E_2|>E_C$, the trajectories $\phi(t)$ oscillate around $n\pi$, where $\sin\phi$ changes its sign and thus the director deflection amplitude $\varphi(t)\propto\sin\phi(t)$ alternates with the electric field (dielectric regime). A similar situation as that shown in Fig. 4(a) is found in general when

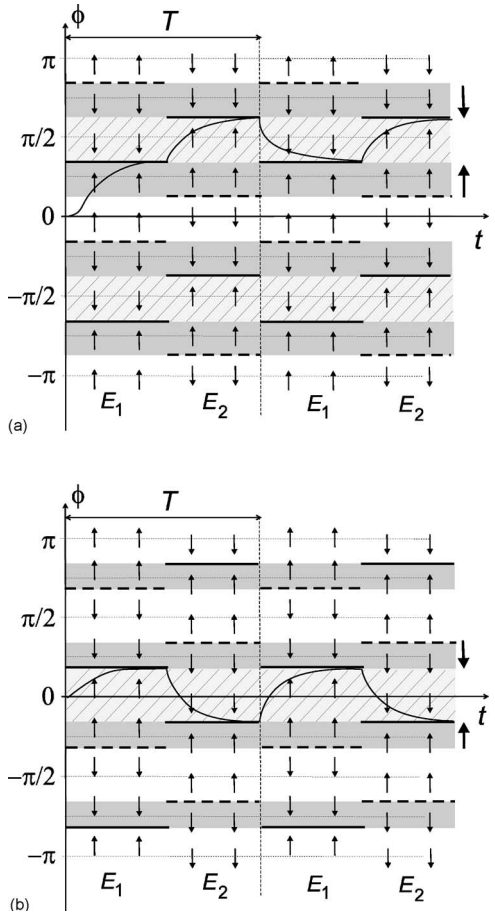

FIG. 4. The figures show schematically two possible structures of the flow of $\phi(t)$ when the excitation waveform is composed of two constant electric fields E_1 and E_2, for the case $\varepsilon_a<0$. (a) absolute values of both fields are below the E_C curve, $0<E_1<E_C$ and $-E_C<E_2<0$ for a given $k_x<k_d$; (b) $k_x>k_d$ or both $E_1>E_C$ and $-E_C>E_2$. Solid lines mark stable fixed points, dashed lines mark unstable fixed points of ϕ. The grey areas are regions with unidirectional flow, hatched areas have only inflow at the borders. The latter trap the trajectories of $\phi(t)$ (exemplary trajectories are sketched).

$|\phi_S(E_1)-\phi_S(E_2)|>\pi/2$, a situation as that shown in Fig. 4(b) is found when $|\phi_S(E_1)-\phi_S(E_2)|<\pi/2$. We note that for stochastically driven EHC, it has been demonstrated earlier by similar arguments [19] that the trajectories cannot rotate in $(\hat{q},\varphi)$ space when the excitation field is dichotomous.

One prerequisite for subharmonic solutions of the differential equation system is that both dynamic variables have to change their signs after one excitation period ($\mu_1<0$). A confinement of ϕ to two quadrants as in Figs. 4(a) and 4(b) generally excludes the existence of subharmonic solutions of the standard EHC system.

If, however, one applies an appropriate excitation scheme consisting of at least three constant voltages to the nematic, it is in principle possible to rotate the trajectories continuously so that all four quadrants are passed during two cycles of the excitation. After one period T of the excitation, the trajectory is in a range of ϕ where both dynamic variables have changed their signs (Fig. 5). With a rearranged excitation sequence, it is possible to rotate ϕ in the opposite sense as well. In all these cases, the asymptotic behavior of $r(t)$ is essential for the stability of the ground state and the definition of the threshold field, so the absence of barriers in the flow map does not necessarily mean that subharmonic patterns are developed, the subharmonic solutions may exist but may not destabilize the ground state if $0>\mu_1>-1$. On the other hand, for all periodic excitation waveforms assembled of only two values for the electric field strength, subharmonic solutions of the differential equation principally cannot exist.

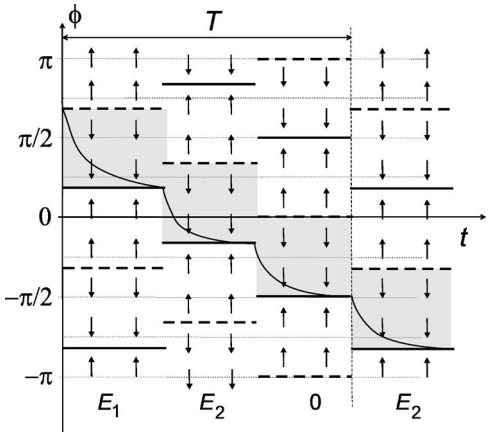

FIG. 5. A possible excitation scheme with three electric field values (trichotomous waveform) $E_1>E_C$, $E_2<-E_C$, and $E_3=0$. An exemplary trajectory is sketched qualitatively.

VII. OTHER EXCITATION WAVEFORMS

From the flow diagram for $\phi(t)$ in Figs. 4(a) and 4(b), it is evident that the statement about dichotomous waveforms can be generalized. We consider the situation in Fig. 4(b) and extend it to arbitrary sequences composed of steps with constant electric field E_i. Gaps with unidirectional flow around $\phi=\pm\pi/4$ also persist when the $\phi_S(E_i)$ of all individual steps are distributed within a range smaller than $\pi/2$. We consider, for example, the case $\varepsilon_a<0$: for any given wave number $k_x>k_d$ of the test mode, the ϕ_S at arbitrary electric fields are in the range $-\pi/4<\phi_S<\pi/4$ [Fig. 3(d)]. Thus subharmonic solutions cannot occur in that wave number region for any excitation waveform. They may only be found in the region $0<k_x<k_d$ when the electric excitation field is appropriately constructed so that E adopts values above as well as below the E_C curve in Fig. 2. This argument holds not only for piecewise constant, but also for arbitrary continuous or discontinuous waveforms. For materials with $\varepsilon_a>0$, the existence of subharmonic solutions is restricted to wave numbers $k_x>k_d$ by the same arguments [see Fig. 3(a)].

In the special case when the nematic material has zero dielectric anisotropy $\varepsilon_\parallel=\varepsilon_\perp$, the two diagonal elements of the matrix $\mathbf{A}(t)$ become time independent. The line $E_C(k_x)$ in Fig. 2 that separates regions of opposite signs of $a_{11}-a_{22}$ becomes exactly vertical, i.e., for any test mode k_x, the difference $a_{11}-a_{22}$ has the same sign independent of the electric

field. In that case, the denominator in Eq. (12) for a given test mode has the same sign for all field strengths. With the arguments given in the previous paragraph, one has to conclude that ϕ remains confined to two or less quadrants for any excitation and any test mode. For a material with isotropic dielectric properties, one can thus exclude the existence of subharmonic solutions of the ODE system completely for arbitrary excitation waveforms. For the formation of subharmonic solutions, it is essential that the electric field enters the diagonal elements of the evolution matrix.

The above discussions do not exclude that further conditions can be formulated which lead to the inhibition of subharmonic solutions of the EHC model equations. However, the three criteria allow us to decide *a priori* for a large ensemble of periodic waveforms whether or not subharmonic solutions can be excluded in general.

For waveforms which lack the above discussed symmetry properties, the formation of subharmonic patterns depends upon material and cell parameters and cannot be predicted generally. On the other hand, some symmetries have been proven to be compatible with subharmonic patterns. For example, the sawtooth waveform has the symmetry $E(t)=-E(T-t)$, and subharmonic patterns have been found experimentally in a certain frequency range for that excitation [12]. In addition, superposition of sine or square waves with even integer frequency ratios can produce subharmonic patterns if frequencies and amplitudes are chosen properly and the mutual phase shift of the superimposed waves is chosen such that the time inversion symmetry is broken (see below).

VIII. NUMERICAL RESULTS

The trajectories of the system variables can be calculated analytically only in a few special situations, in particular if the waveforms consist of piecewise constant segments. In general, one has to solve the equations numerically. The following chapter shows the structure of the stability diagrams for a few selected typical situations. For the construction of these stability diagrams (Fig. 6 and following), a sufficiently fine grid of the two parameters (e.g., wave number and electric field amplitude) is chosen. For each parameter set, two independent initial vectors $\vec{Z}_1(0)$, $\vec{Z}_2(0)$ are chosen, and their evolution is calculated for a full excitation period by solving Eq. (2). From the results $Z_1(T)$, $Z_2(T)$, the eigenvectors and eigenvalues of **M** are obtained.

We present the Floquet multiplier μ_1 as a function of the test mode wavelength and a selected electric field strength parameter characterizing the excitation. In the numerical calculations, we use the data of the material *Mischung 5* [11,12] which has been studied in previous experiments. If not otherwise indicated, $\sigma_\parallel=96\ \mathrm{s}^{-1}$ (cgs, esu), $\gamma_1=3.65\ \mathrm{g\ cm}^{-1}\ \mathrm{s}-1$ (cgs), $\varepsilon_\parallel=5.6$, $\varepsilon_\perp=6.0$. With this set of material parameters, one has $k_d=0.735\ \mu\mathrm{m}^{-1}$. We assume a cell thickness of $d=48.5\ \mu$m. This is the thickness of the cell used in the experiments in Sec. IX.

Of course, such numerical results can only positively prove the existence of subharmonic solutions. Their absence in the numerical results is only an indication that subharmonic solutions do not exist for a given excitation waveform, because their existence ranges depend in detail upon the choice of a particular set of material parameters. Nevertheless, the numerical data may be appropriate to support the above made statements.

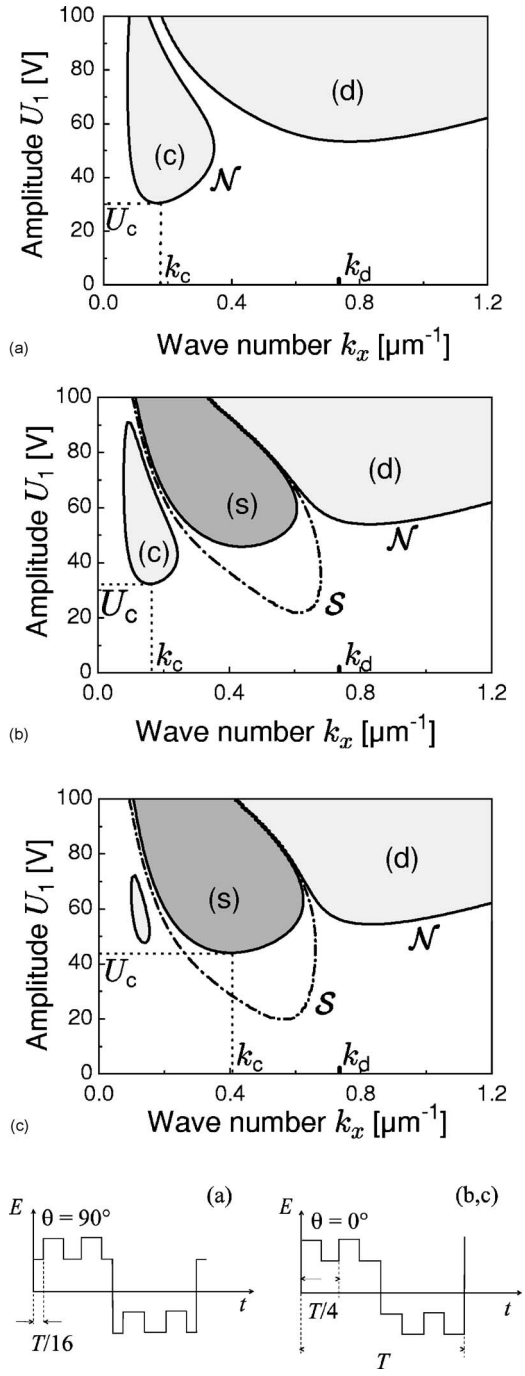

FIG. 6. Numerical calculated stability diagrams for superposition of rectangular waves with frequency ratio 1:4, $f_1=30$ Hz, $f_2=120$ Hz, and with phase shifts of $\theta=90°$ (a) and $\theta=0°$ (b), (c), see graphs at the bottom. The vertical axis is the amplitude of the low frequency voltage, $U_1=E_1 d$. Regions with $|\mu_1|>1$ are shaded. Labels denote conduction (*c*), subharmonic (*s*), and dielectric (*d*) patterns. The high frequency voltage amplitudes are $U_2=30$ V (a), (b) and $U_2=39$ V (c).

First, we refer to the numerical results published in Ref. [12] where triangular wave excitation has been discussed. In that paper, stability diagrams have been presented for a strictly antisymmetric excitation with the triangular waveform

$$E(t) = \begin{cases} (4t/T)E_0 & \text{for } 0 \leqslant t < T/4, \\ (2-4t/T)E_0 & \text{for } T/4 \leqslant t < 3T/4, \\ (4t/T-4)E_0 & \text{for } 3T/4 \leqslant t < T, \\ E(t \bmod T) & \text{elsewhere}, \end{cases} \tag{15}$$

which fulfills the condition of Sec. IV. The stability diagrams show that only conduction and dielectric regimes are formed while the tongue of subharmonic solutions is missing completely in the stability diagram, μ_1 is non-negative everywhere. In contrast, a region with subharmonic solutions is found for certain nonsymmetric triangular waveforms

$$E(t) = \begin{cases} (t/T_s)E_0 & \text{for } 0 \leqslant t < T_s, \\ [(T/2-t)/(T/2-T_s)]E_0 & \text{for } T_s \leqslant t < T-T_s, \\ [(t-T)/T_s]E_0 & \text{for } T-T_s \leqslant t < T, \\ E(t \bmod T) & \text{elsewhere}, \end{cases} \tag{16}$$

with $T/4 < T_s \leqslant T/2$. Subharmonic solutions exist in a given parameter range and a subharmonic island with $\mu_1 < -1$ can even provide the global minimum of the neutral curve ($|\mu_1| = 1$) so that subharmonic patterns form at onset of the instability.

Other typical examples are excitations with superimposed square waves with even and odd frequency ratios. The subharmonic tongue is missing completely when two electric square waves with odd frequency ratio are superimposed, while it is present in situations where the two superimposed square waves have an even frequency ratio and none of the inhibiting conditions given in Secs. V–VII is fulfilled. It has been shown experimentally as well as theoretically already in Ref. [11] that with certain parameter sets, subharmonic patterns may form the first instability.

In order to test the time inversion symmetry condition, we choose a superposition of square waves with even frequency ratio and different phase shifts between the two frequencies. We define the phase shift by the position of the first positive slope of the high-frequency component following a positive slope of the low frequency component, measured in units of the period of the high-frequency component.

Figure 6 shows the exemplary stability diagrams for superposition of two square waves (E_1, f_1) and (E_2, f_2), with 1:4 frequency ratio. $\mathcal{N}$ is the neutral curve, where $|\mu_1| = 1$ and $\mathcal{S}$ marks the separatrix where the real parts of $\mu_{1,2}$ change their signs. Dark shaded areas mark regions with $\mu_1 < -1$, bright shaded areas correspond to $\mu_1 > 1$. In these shaded areas, the nonconvecting ground state is instable with respect to conduction (c), subharmonic (s), or dielectric (d) patterns. The voltages U_i are given by $E_i d$.

In Fig. 6(a), the phase shift is 90°, and the excitation has time reversal symmetry. The subharmonic tongue is completely absent for any choices of material and geometry parameters. In Figs. 6(b) and 6(c), the phase shift is zero and the time inversion symmetry is broken. In the stability diagram of Fig. 6(b), a subharmonic tongue is found, but does not provide the global minimum of the neutral curve for the given parameter set. With the parameters chosen in Fig. 6(c), the global minimum of $\mathcal{N}$ lies on the border of the subharmonic tongue and subharmonic patterns provide the threshold for pattern onset. The experimental confirmation is given in the next section. In all pictures, we have marked the wave number k_d where the theoretical E_C curve intersects the k_x axis. As discussed in the previous section, subharmonic patterns can be expected only at wave numbers smaller than k_d for the particular material with negative dielectric anisotropy.

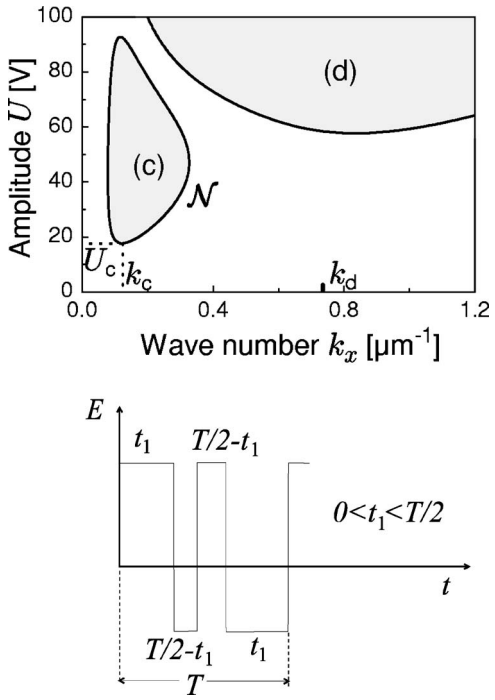

FIG. 7. Calculated stability diagram for excitation with a dichotomous waveform (see text and graph at the bottom) that lacks the time symmetries discussed in the previous sections, $t_1 = T/3$, $f = 1/T = 20$ Hz.

Figure 7 shows a typical stability diagram for a waveform composed of two electric field values $\pm E_0$,

$$E(t) = E_0 \,\mathrm{sgn}[\sin(2\pi f t) + \sin(4\pi f t)], \tag{17}$$

where the condition of Sec. VI (dichotomous function) is fulfilled but none of the other conditions. The tongue with subharmonic solutions is absent. In contrast, such a tongue of subharmonic solutions can be found for waveforms composed of three or more electric field values, as is demonstrated in Fig. 8. The waveform used in the computation of that stability diagram was

$$E(t) = E_0\{\mathrm{sgn}[\cos(2\pi f t)] + \mathrm{sgn}[\sin(4\pi f t)]\}. \tag{18}$$

The detailed structure of the stability diagram depends upon the frequency $f = 1/T$ of the excitation. The subharmonic tongue is present at all frequencies tested in our numerical calculations, whereas the global minimum of the neutral

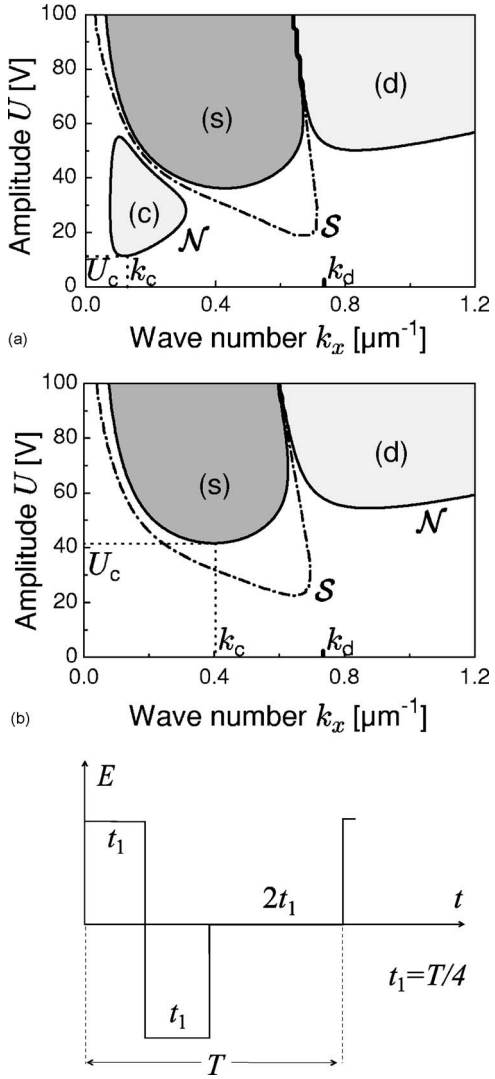

FIG. 8. Calculated stability diagram for rectangular wave excitation with the shape shown in the bottom graph. It lacks the time symmetries discussed in the previous sections. A subharmonic tongue is formed. Sawtooth excitation, $f=1/T=25$ Hz (a) and 35 Hz (b).

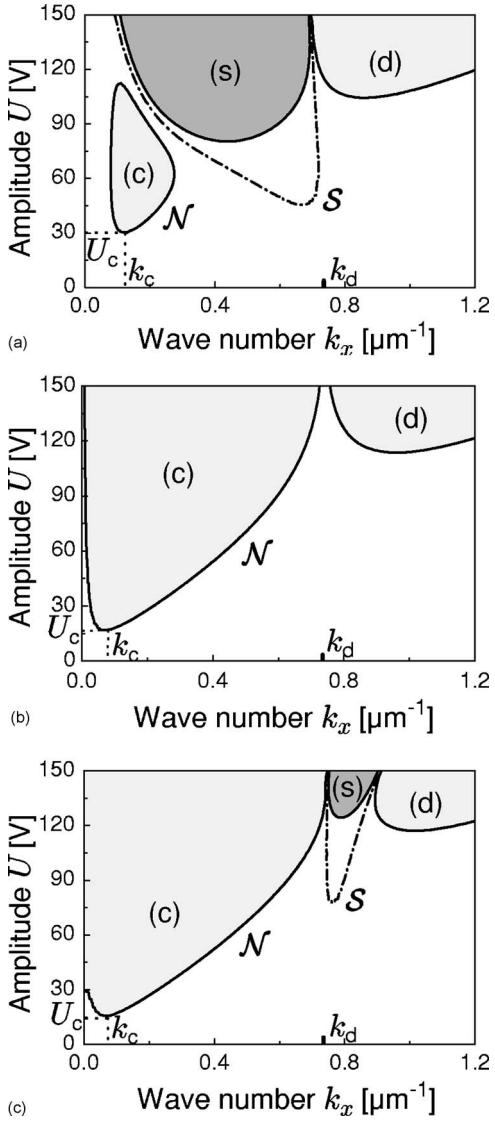

FIG. 9. Calculated stability diagrams for sawtooth excitation, $\varepsilon_\perp=6.0$ (a), $\varepsilon_\perp=5.6$, (b), and $\varepsilon_\perp=5.55$ (c). $\varepsilon_\parallel=5.6$ in all cases.

curve is provided by the subharmonic structures only in a certain frequency interval, as in the case of sawtooth excitation.

Figure 9 compares the stability diagram for a material with $\varepsilon_a=0$ (b) with two cases $\varepsilon_a<0$ (a) and $\varepsilon_a>0$ (c). With $\varepsilon_a=0$ [Fig. 9(b)] the two diagonal elements a_{22} and a_{11} are both time independent, subharmonic solutions cannot exist as derived in Sec. VI. The border between the region of conduction roll-like solutions (φ varies around $\pi/2$) and dielectric roll-like solutions (φ varies around 0) is a vertical in the image starting at k_d. Note also that the subharmonic solutions appear for test modes with $k_x>k_d$ in the case $\varepsilon_a>0$ [Fig. 9(c)], and in the range $k_x<k_d$ in the case $\varepsilon_a<0$ [Fig. 9(b)], as we had predicted from the model.

In addition to the stability diagrams, numerically calculated trajectories support the predictions of the analytical model. The restriction of ϕ to two quadrants in the case of dichotomous waveforms can be seen from Fig. 10(a), where $q(\varphi)$ is presented exemplarily for the dichotomous waveform of Eq. (17), Fig. 7 at (U_c,k_c). For comparison, the calculated trajectory in the case of the trichotomous waveform of Eq. (18), Fig. 8(b) at (U_c,k_c) is shown in Fig. 10(b). It passes all quadrants in the subharmonic regime.

IX. EXPERIMENT

Figure 11 shows different structures in the subharmonic regime (b)–(d), and for comparison, normal rolls in the conduction regime of the same cell (a). All photos are instant images (exposure time shorter than the period of the excitation). Time averaged optical textures of the subharmonic patterns in (b)–(d), as seen by eye, have half the wave length of the spatial director pattern, since the pattern shifts by a half wavelengt after each period of the excitation. The chevron formation seen in images 11c,d is very similar to what one observes in the dielectric regime.

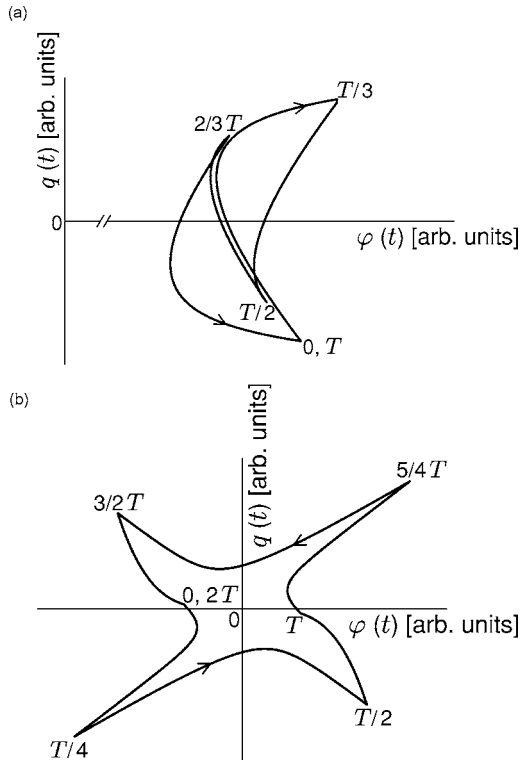

FIG. 10. (a) Calculated trajectories in the (q,φ) plane for the dichotomous waveform of Fig. 7 at the critical (U_c,k_c). The trajectory is restricted to two quadrants of the (q,φ) space. There exists a second, separate branch in the other two quadrants which is found by inversion of the signs of both q and φ. (b) Calculated trajectories for the waveform of Fig. 8(b), the corresponding trajectory at (U_c,k_c) in the subharmonic range passes cyclically through all four quadrants within the time period $2T$.

For an identification of subharmonic dynamics, these images are not sufficient. Even though the agreement of critical voltages and wavelengths measured in the experimental with the numerical predictions is a strong indication for subharmonic patterns, a strict experimental confirmation of their dynamics is only possible in the spatiotemporal analysis. The Floquet multiplier of -1 for the subharmonic patterns can always be compensated by a spatial shift of the pattern by half a director period. Thus, the subharmonic nature of the dynamics is not discernible in integral signals such as diffraction intensities or the electric current through the cell.

As well as the numerical results given in the previous section, experiments cannot prove the absence of subharmonic patterns. The latter can only demonstrate the presence of subharmonic patterns when these form the first instability. However, all experiments performed confirm the predictions of the model and show that the model is not only appropriate for the description of the fundamental time symmetries of the pattern dynamics but it describes also, with great detail, the trajectories of φ [11,12,35]. This has been done for two special cases already in previous publications, for the superposition of phase shift free rectangular waves with an even frequency ratio, it has been shown that subharmonic patterns appear in a certain frequency range. The stability diagrams and trajectories of the dynamic variables have been given

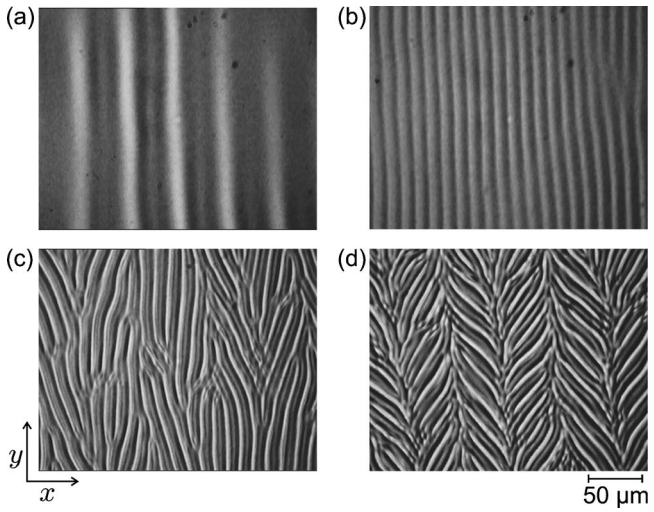

FIG. 11. EHC patterns at sawtooth excitation: (a) normal rolls in the conduction regime 60 Hz, 42.1 V, (b) normal rolls in the subharmonic regime 76 Hz, 128.45 V, (c) chevron formation in the subharmonic regime 80 Hz, 153.65 V, (d) chevrons in the subharmonic regime 80 Hz, 165.1 V.

and the comparison with the experiment has been performed on the basis of the time-dependent laser diffraction intensity and evaluation of the pattern wavelengths [11]. In a subsequent paper, it has been shown that for a much simpler excitation waveform, the sawtooth, subharmonic patterns are experimentally observable, the observation technique has been improved there so that the time dependent pattern dynamics could be directly recorded with a high-speed camera [12]. In that study, the experimental thresholds have been measured not only for the sawtooth [Eq. (16) with $T_s=T/2$], and the antisymmetric triangle [Eq. (15)], but also for the general case of Eq. (16), and a transition behavior has been observed with increasing deviation from the antisymmetry of the excitation.

We extend these experiments here to the conditions of Sec. V by studying the superposition of square waves at a frequency ratio 1:4, with and without a mutual phase shift. We use the material *Mischung 5*, its chemical composition, phase transition temperatures and material parameters can be found, e.g., in Refs. [11,12]. As seen in Fig. 6, the numerical analysis confirms the absence of the subharmonic tongue when the phase shift is 90° and the excitation is time antisymmetric. In this experiment, three parameters can be adjusted, the frequency f_1 and the two voltage amplitudes $U_1=E_1d$, $U_2=E_2d$ of the low- and high-frequency components. In the experiment, U_1 is increased at fixed U_2 until the homogeneous ground state vanishes and the first convection pattern appears. An exception is the right hand slope of the threshold curve (see Fig. 12) where U_1 is kept constant and U_2 is varied to find the threshold. The first frequency f_1 is chosen below the cutoff frequency for square wave excitation, and the second frequency $f_2=4f_1$ lies above the cutoff, thus the threshold curve intersects the U_1 and U_2 axes at the threshod voltages for conduction and dielectric patterns, respectively, for pure square wave excitation. The bifurcation is forward in all parts of the curve, the pattern onset is nonhysteretic.

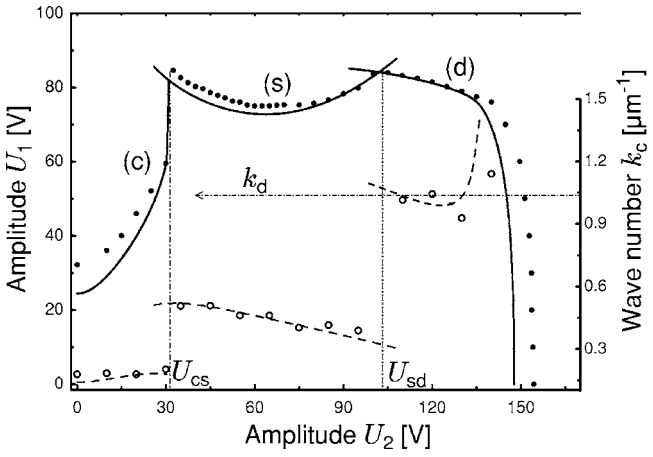

FIG. 12. Plot of the experimentally determined thresholds at superposition of two square waves (solid circles). The frequencies are $f_1=80$ Hz, $f_2=320$ Hz. The solid line is the numerically calculated threshold curve, where $\sigma_\parallel=185$ s^{-1} and $\gamma_1=3.62$ g cm^{-1} s^{-1} have been fitted. The open symbols represent the measured critical wavelengths, the dashed line is the calculated curve. Note that all critical wavelengths are below $k_d=1.04$ μm^{-1} in the subharmonic regime, as predicted.

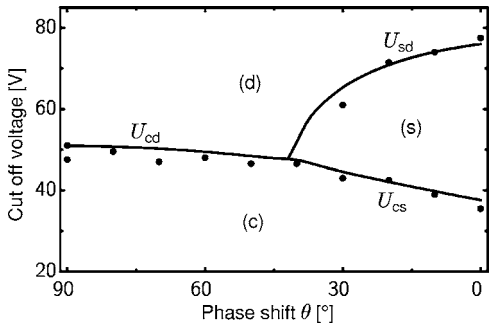

FIG. 13. Plot of the experimentally determined transitions between the conduction, subharmonic and dielectric regimes (dots) at superposition of two square waves with phase shift θ. The solid lines depict the prediction from the numerical solution of the model differential equation system. Frequencies are $f_1=30$ Hz, $f_2=120$ Hz. Note that the choice of different f_1, f_2 compared to Fig. 12 has no qualitative consequences on the threshold diagram provided the same frequency ratio and phase shift θ are maintained and f_1, f_2 are chosen below and above the cutoff for pure rectangular wave excitation, respectively.

Figure 12 shows a typical threshold curve measured for zero phase shift. At low amplitudes of the high-frequency component U_2, the instability is towards conduction patterns (normal rolls), at high voltages of the high frequency component, the instability is towards dielectric rolls, and at an intermediate voltage range, the subharmonic patterns provide the first instability. Similar results have been presented in Ref. [11]. The numerically calculated stability diagrams are qualitatively similar to those depicted in Figs. 6(b) and 6(c). At the two voltages U_{cs} and U_{sd} of the high-frequency component, the first instability changes from conduction to subharmonic patterns and from subharmonic to dielectric patterns, respectively. Small quantitative deviations of the theoretical threshold curves in the plot of Fig. 12 may reflect the limits of the model for an exact quantitative description. It has been discussed in the introduction that more elaborate, more complex mathematical models exist which yield qualitatively equivalent results but may give a slightly better fit of the threshold curves in some situations.

According to the considerations in Sec. V, the subharmonic patterns should vanish if the phase shift θ between the two superimposed frequencies reaches 90°. One expects the "classical" direct transition from conduction to dielectric patterns at U_{cd}. Consequently, we have varied the phase shift between the two superimposed rectangular waves, at fixed frequencies f_1 and $f_2=4f_1$, in steps from 90° to 0°. Figure 13 shows a diagram of the transition voltages U_{cd}, U_{cs}, and U_{sd} as a function of the phase shift θ between the two components. In agreement with the model, subharmonic patterns are not observed when the phase shift is $\theta=90°$. When $\theta\neq 90°$, the time reversal symmetry is broken and the subharmonic tongue forms in the stability diagram. This tongue does not provide the global minimum of the neutral curve when θ is in the vicinity of 90°. When the phase shift between the two superimposed excitation waves reaches some critical value, the subharmonic patterns are seen experimentally, and their existence range is largest at $\theta=0$. The experimental situation is symmetric with respect to the substitutions $\theta\rightarrow-\theta$ and $\theta\rightarrow 180°-\theta$. The numerical results are in excellent qualitative agreement and even in satisfactory quantitative agreement with the measurements, as is shown by the solid line in Fig. 13.

It is noticeable that in this excitation scheme, the frequency spectra of excitations for different θ are equivalent except for phase factors. The disappearance of the subharmonic patterns at $\theta=90°$ has to be attributed exclusively to the particular time symmetry of the excitation. Time scales related with dynamical properties of the material cannot be used to explain the qualitative differences between threshold curves for different θ.

X. CONCLUSIONS

We have derived some fundamental relations between symmetries of the electric excitation fields and the time response of the electroconvection patterns in nematic cells. Only patterns described by the Carr-Helfrich mechanism have been considered, which are the most comprehensively investigated convection structures in liquid crystals. Certain symmetries of the dynamic equations lead to fundamental consequences for the pattern dynamics.

It has been shown analytically that three conditions can be formulated for the symmetries of the excitation waveforms that inhibit the formation of subharmonic patterns in EHC. Subharmonic patterns are excluded when at least one of the following conditions is fulfilled. (i) The excitation $E(t)$ is antisymmetric with respect to a shift of one half excitation period in time $E(t)=E(t+T)=-E(t+T/2)$. (ii) The excitation $E(t)$ is symmetric with respect to time reversal, i.e., there exist certain t_0 for which $E(t)=E(t+T)=E(t_0-t)$. (iii) The excitation is dichotomous, i.e., it consists of segments of

constant electric field strength and the driving field adopts only the two values $E_1 \neq E_2$.

Obviously, the first conclusion is generally valid for a two-variable dynamic system with the structure of Eq. (2) when the two off-diagonal elements of the matrix $\mathbf{A}(t)$ are odd functions and the diagonal elements are even functions of the driving parameter E, $a_{ij}(E)=a_{ij}(-E)$ for $i=j$, and $a_{ij}(E)=-a_{ij}(-E)$ for $i \neq j$, with $i,j=\{1,2\}$. The second conclusion holds for any similar dynamic system where the two off-diagonal elements have the same dependence on the driving parameter E and differ only by a constant factor $a_{12}(E)=\text{const}\, a_{21}(E)$.

Furthermore, it is necessary that the liquid crystal material has a nonzero dielectric anisotropy ε_a in order to produce subharmonic solutions of the differential equation system. If the material is dielectrically anisotropic, the sign of ε_a determines in which part of the stability diagram (k_x above or below k_d) the subharmonic solutions can form. In a more general formulation, the subharmonic patterns are not present at any periodic excitation if the diagonal elements of $\mathbf{A}$ are independent of the driving field $E(t)$.

These analytical predictions have been tested by numerical calculations of stability diagrams and threshold curves. Experimental data have been presented in this study that support the second condition. Experiments supporting the first condition had already been provided earlier [12]. Similar experiments could be performed in support of the third prediction by the investigation of arbitrary periodic dichotomous waveforms, but such experiments can on principle never verify the theoretical prediction. In order to test the last prediction of our model, it is possible to prepare a material with $\varepsilon_a=0$, by slightly modifying the concentrations of the four components of *Mischung 5* (increasing the content of the compound with the cyano substituent). Then, one may test that subharmonic patterns are absent at arbitrary excitations. This requires, however, an extensive preparational effort. It might be a subject of future experimental studies.

Within this linear analysis, only statements about the patterns at onset can be made, above the threshold, the situation is far more complex and neither experimental nor theoretical data are available so far that support or contradict the appearance of subharmonic patterns for general periodic waveforms far from the thresholds. Furthermore, we have neglected possible flexoelectric terms that can modify the symmetries of the pattern response, in particular when hybrid anchoring conditions at the two cell plates are assumed.

ACKNOWLEDGMENTS

One of the authors (J.H.) acknowledges support by the Landesstipendium Sachsen-Anhalt.

APPENDIX: MATRIX COEFFICIENTS

The coefficients in Eq. (2) in the cgs system are given by [19]

$$A_1 = -4\pi \frac{\sigma_\parallel k_x^2 + \sigma_\perp k_z^2}{\varepsilon_\parallel k_x^2 + \varepsilon_\perp k_z^2},$$

$$A_2 = +\frac{(\sigma_\parallel \varepsilon_\perp - \varepsilon_\parallel \sigma_\perp)(k_x^2 + k_z^2)}{\varepsilon_\parallel k_x^2 + \varepsilon_\perp k_z^2} k_x,$$

$$A_3 = +\frac{1}{f}\left[\frac{1}{2}\frac{(\gamma_1-\gamma_2)k_x^4 + (\gamma_1+\gamma_2)k_x^2 k_z^2}{\alpha_1 k_x^2 k_z^2 + (k_x^2+k_z^2)(\eta_1 k_x^2 + \eta_2 k_z^2)} - \frac{\varepsilon_a k_x^2}{\varepsilon_\parallel k_x^2 + \varepsilon_\perp k_z^2}\right]\frac{1}{k_x},$$

$$A_4 = -\frac{K_{33}k_x^2 + K_{11}k_z^2}{f},$$

$$A_5 = +\frac{1}{f}\left[\frac{\varepsilon_a \varepsilon_\perp (k_x^2+k_z^2)}{4\pi(\varepsilon_\parallel k_x^2 + \varepsilon_\perp k_z^2)}\right],$$

with $k_z=\pi/d$, $\varepsilon_a=\varepsilon_\parallel-\varepsilon_\perp$ and the abbreviation

$$f = \gamma_1 - \frac{1}{4}\times\frac{[(\gamma_1-\gamma_2)k_x^2 + (\gamma_1+\gamma_2)k_z^2]^2}{\alpha_1 k_x^2 k_z^2 + (k_x^2+k_z^2)(\eta_1 k_x^2 + \eta_2 k_z^2)},$$

with the elastic constants K_{11} and K_{33} of the nematic, the rotational viscosity γ_1, viscosities α_1, γ_2, η_1, the components $\varepsilon_\parallel$, $\varepsilon_\perp$ of the dielectric tensor parallel and perpendicular to the director, respectively, and $\varepsilon_a=\varepsilon_\parallel-\varepsilon_\perp$. The conductivities of the material parallel and perpendicular to the director are $\sigma_\parallel$ and $\sigma_\perp$, respectively, and $\vec{k}$ is the wave vector of the convection rolls.

Most of the material parameters are accessible by independent experiments and have been determined earlier. The conductivities vary from cell to cell, therefore we use $\sigma_\parallel$ as a fitting parameter (it essentially determines the cutoff frequency), keeping the ratio $\sigma_\parallel/\sigma_\perp$ fixed.

[1] R. Williams, J. Chem. Phys. **39**, 384 (1963); A. P. Kapustin and L. K. Vistin, Kristallografiya **10**, 118 (1965).

[2] E. F. Carr, J. Chem. Phys. **38**, 1536 (1963).

[3] W. Helfrich, J. Chem. Phys. **51**, 4092 (1969).

[4] See, e.g., E. I. Butikov, J. Phys. A **35**, 6209 (2002), and references therein.

[5] M. Faraday, Philos. Trans. R. Soc. London **52**, 319 (1831).

[6] W. S. Edwards and S. Fauve, C. R. Acad. Sci., Ser. II: Mec., Phys., Chim., Sci. Terre Univers **315**, 417 (1992).

[7] A. Kudrolli and P. Gollub, Physica D **97**, 133 (1996); **123**, 99 (1998).

[8] H. Arbell and J. Fineberg, Phys. Rev. Lett. **81**, 4384 (1998), Phys. Rev. E **65**, 036224 (2002).

[9] H. W. Müller, H. Wittmer, C. Wagner, J. Albers, and K. Knorr, Phys. Rev. Lett. **78**, 2357 (1997).

[10] For a review see, e.g., J. Miles and D. Henderson, Annu. Rev.

Fluid Mech. **22**, 143 (1990); H. W. Müller, R. Friedrich, and D. Papathanassiou, *Theoretical and Experimental Studies of the Faraday system*, in Vol. M55 of *Lecture Notes in Physics*, edited by F. H. Busse and S. C. Müller, (Springer, Berlin, 1998), p. 230.
[11] Th. John and R. Stannarius, Phys. Rev. E **70**, 025202(R) (2004).
[12] Th. John, J. Heuer, and R. Stannarius, Phys. Rev. E **71**, 056307 (2005).
[13] T. P. Schulze, Phys. Fluids **11**, 3573 (1999).
[14] Orsay Liquid Crystal Group, Phys. Rev. Lett. **26**, 1642 (1970).
[15] E. Dubois-Violette, P. G. de Gennes, and O. Parodi, J. Phys. (France) **32**, 305 (1971).
[16] E. Dubois-Violette, J. Phys. (France) **33**, 95 (1972).
[17] I. W. Smith, Y. Galerne, S. T. Lagerwall, E. Dubois-Violette, and G. Durand, J. Phys. Colloq. **36**, C1–237 (1975).
[18] P. A. Penz and G. W. Ford, Phys. Rev. A **6**, 414 (1972).
[19] U. Behn, A. Lange, and Th. John, Phys. Rev. E **58**, 2047 (1998).
[20] L. Kramer and W. Pesch, Annu. Rev. Fluid Mech. **17**, 515 (1995).
[21] L. Kramer and W. Pesch, in *Pattern formation in Liquid Crystals*, edited by L. Kramer and A. Buka (Springer, New York, 1995), p. 221.
[22] L. Kramer, E. Bodenschatz, W. Pesch, W. Thom, and W. Zimmermann, Liq. Cryst. **5**, 699 (1989).
[23] W. Zimmermann and L. Kramer, Phys. Rev. Lett. **55**, 402 (1985).
[24] E. Bodenschatz, W. Zimmermann, and L. Kramer, J. Phys. (Paris) **49**, 1875 (1988).
[25] E. Plaut, W. Decker, A. G. Rossberg, L. Kramer, W. Pesch, A. Belaidi, and R. Ribotta, Phys. Rev. Lett. **79**, 2367 (1997).
[26] M. Treiber and L. Kramer, Mol. Cryst. Liq. Cryst. Sci. Technol., Sect. A **261**, 303 (1995).
[27] M. Dennin, M. Treiber, L. Kramer, G. Ahlers, and D. S. Cannell, Phys. Rev. Lett. **76**, 319 (1996).
[28] W. Zimmermann, in *Nematics Mathematical and Physical Aspects*, edited by J.-M. Coron, J.-M. Ghidaglia, and F. Hélein (Kluwer, Dordrecht, 1991), p. 401.
[29] W. Pesch and U. Behn, in *Evolution of Spontaneous Structures in Dissipative Continuous Systems*, edited by F. H. Busse and S. C. Müller (Springer, Heidelberg, 1998), p. 335.
[30] A. G. Rossberg and L. Kramer, Physica D **115**, 19 (1998).
[31] Y. Tu, Phys. Rev. E **56**, R3765 (1997).
[32] E. Plaut and R. Ribotta, Phys. Rev. E **56**, R2375 (1997).
[33] For example, I. J. Epstein, Proc. Am. Math. Soc. **13**, 690 (1962); I. J. Epstein, J. Diff. Eqns. **1**, 206 (1965). J. S. Muldowney, Proc. Am. Math. Soc. **18**, 22 (1967).
[34] see, e.g., J. Hale, *Ordinary Differential Equations*, 2nd ed. (Krieger, Malabar, FL, 1980).
[35] C. Bohley, J. Heuer, R. Stannarius, J. Opt. Soc. Am. (to be published).
[36] When flexoelectric effects are taken into account, one finds mixtures of these types of solutions, see, e.g., Ref. [20]
[37] in the case of positive ε_a, one has to consider in addition the threshold for the Fréedericksz transition as a competing instability.